Proceedings of the 16th International Conference on Soil Mechanics and Geotechnical Engineering

doi:10.3233/978-1-61499-656-9-391

Fraser River sand. Mathematical characterization

Description mathématique du comportement d'un sable provenant du Fleuve Fraser

Eulalio Juárez Badillo
Graduate School of Engineering, National University of Mexico

ABSTRACT
General equations provided by the principle of natural proportionality are applied to mathematically characterize the undrained behaviour of Fraser River sand. The undrained tests were carried out using displacement-controlled loading to confidently capture the post-peak strain-softening response. The very good tests, already published, were made to show the dependence of the undrained behaviour of sand on the initial stress state and the orientation of principal stresses with respect to the bedding planes under generalized loading paths using hallow cylinder torsional shear tests. A mere rotation of principal stresses at constant deviator stress alone is included.

RESUMÉ
Les équations générales dérives du Principe de la Proportionnalité Naturelle ont été appliquées pour faire la description mathématique du comportement d'un sable provenant du fleuve Fraser, en conditions non drainées. Les essais non drainées ont été effectues au moyen d'un système de charge en déplacement, permettant de mesures très precises en grandes déformations. Les essais réalisent ont mis en évidence l 'dépendance comportement non-draine du sable testé par rapport à la contrainte de confinement initiale et la rotation des axes principaux du tenseur des contraintes a l'aide des appareils triaxiaux de torsion sur un cylindre creux. Une rotation pure des axes principaux du tenseur des contraintes sous un déviateur de contrainte constant a été rapporte.

1 INTRODUCTION

The dependence of the undrained behaviour of sand on the initial stress state and the orientation of principal stresses with respect to the bedding planes is assessed under generalized loading paths using hallow cylinder torsional shear tests. The very good and interesting tests have already been published (Sivathayalan and Vaid 2002). The author read it with great interest and immediately was tempted to apply the general equations provided by the principle of natural proportionality (Juarez-Badillo 1999 a, b) to mathematically describe such behaviour. The results are the subject of this paper.

The author highly suggest to the reader to read first such a paper where all details on test apparatus and experimentation are given and the test results are commented. All experimental figures in this paper are from such reference. All what the author has made is to include in such figures theoretical points given by the different theoretical equations used.

2 THEORETICAL EQUATIONS

It is highly useful to have at hand the graphs of the different equations used to describe such experimental behaviour, that is the reason the author decided to include such graphs in this paper. Fig. 1 shows the pre-peak sensitivity function Y_S given by

$$Y_S = \frac{\sigma_1 - \sigma_3}{(\sigma_1 - \sigma_3)_f} = \left[1 + \left(\frac{e_a}{e_a^*}\right)^{-1/\nu}\right]^{-1} \tag{1}$$

where σ_1 - σ_3 maximum deviator stress, e_a = axial deviatoric natural strain, $(\sigma_1 - \sigma_3)_f$ = final $(\sigma_1 - \sigma_3)$ at $e_a = \infty$, e_a^* = characteristic e_a at $(\sigma_1 - \sigma_3)$ = ½ $(\sigma_1 - \sigma_3)_f$ and ν = shear exponent.

Fig. 2 shows the pre-peak inverted function Y_I given by

$$Y_I = \frac{\sigma_1 - \sigma_3}{(\sigma_1 - \sigma_3)^*} = \left[\left(\frac{e_a}{e_{af}}\right)^{-1} - 1\right]^{-1/\nu} \tag{2}$$

where $(\sigma_1 - \sigma_3)^*$ = characteristic $(\sigma_1 - \sigma_3)$ at e_a = ½ e_{af} and e_{af} = final e_a at $(\sigma_1 - \sigma_3) = \infty$.

Fig. 3 shows the post-peak ductility function Y_D given by

$$Y_D = \frac{(\sigma_1 - \sigma_3) - (\sigma_1 - \sigma_3)_\infty}{(\sigma_1 - \sigma_3)_1 - (\sigma_1 - \sigma_3)_\infty} = \left(\frac{e_a}{e_{a1}}\right)^{-1/\nu} \tag{3}$$

where $(\sigma_1 - \sigma_3)_\infty$ = $(\sigma_1 - \sigma_3)$ at $e_a = \infty$ and $(e_{a1}, (\sigma_1 - \sigma_3)_1)$ is a known point.

Fig. 4 shows the sensitivity function Y given by

$$Y = \left[1 + \left(\frac{e_a}{e_a^*}\right)^{-\beta}\right]^{-1} \tag{4}$$

where $e_a^* = e_a$ at Y = ½ and β is a constant. Observe that Y varies from 0 to 1 when e_a varies from 0 to ∞.

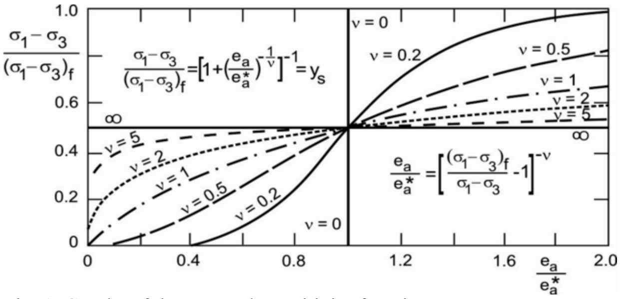

Fig. 1. Graphs of the pre-peak sensitivity function Y_S

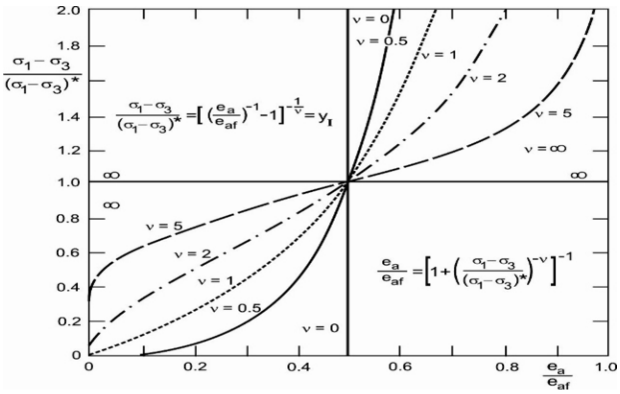

Fig. 2. Graphs of the pre-peak inverted function Y_I

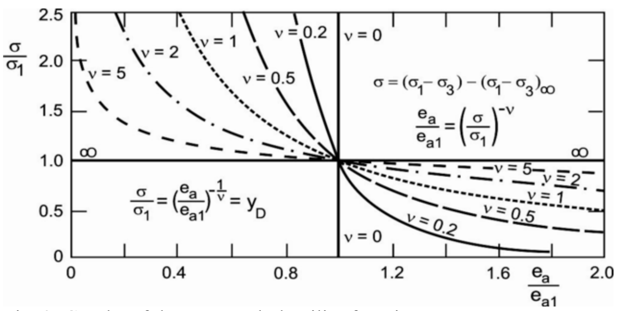

Fig. 3. Graphs of the post-peak ductility function Y_D

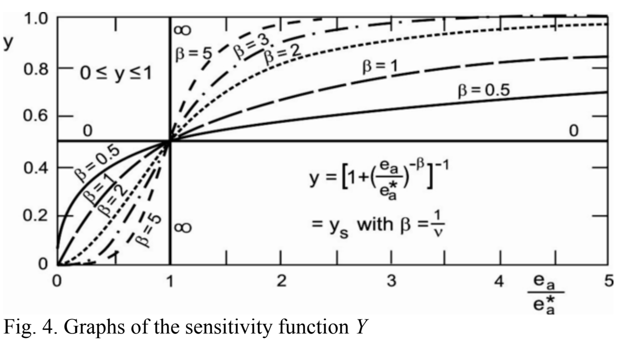

Fig. 4. Graphs of the sensitivity function Y

The pore pressure Δu in undrained tests is given by

$$\Delta u = \Delta\sigma_i + \alpha\sigma_{co}Y - \alpha_e\left(\sigma_{eo} - \sigma_{co}\right)Y_e \tag{5}$$

where $\Delta\sigma_i$ = isotropic stress increment, σ_{co} = initial isotropic consolidation pressure, σ_{eo} = initial isotropic equivalent consolidation pressure due to interlocking, α and α_e = constant pore pressure coefficients ($0 \leq \alpha \leq 1$). The sub-index e in α and Y in the third terms is just to distinguish them from α and Y in the second term.

3 PRACTICAL APPLICATION

Fig. 5 shows the response of laboratory water-pluviated identical specimens of loose Fraser River sand in undrained extension and compression. The UC experimental curves indicate they are of the pre-peak inverted function type Y_I. Equation (2) was applied considering that the Cauchy common axial strain ε_a is very close to the axial deviatoric natural strain e_a due to their small values (ε_a < 8%). The parameters to be determined are v, e_{af} and $(\sigma_1 - \sigma_3)^*$. They can mathematically be determined from three good experimental points in each curve. However, the author preferred a trial and error procedure. Observe that for any e_{af} shosen corresponds a given $(\sigma_1 - \sigma_3)^*$. After a trial and error procedure the author found the values shown in Table 1.

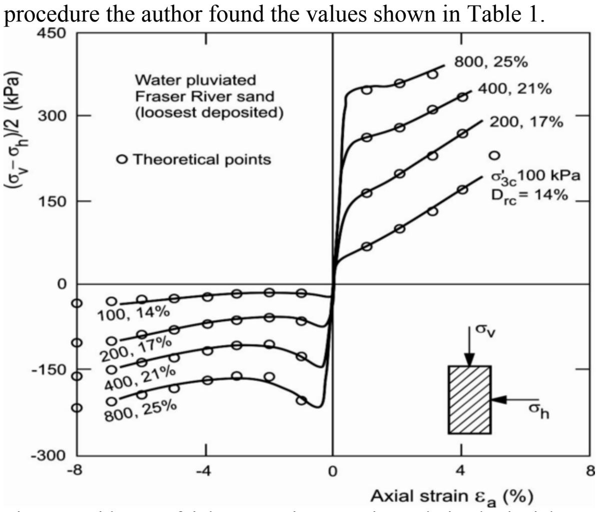

Fig. 5. Evidence of inherent anisotropy in undrained triaxial tests (after Vaid and Thomas, 1995). D_{rc} relative density at the end of consolidation; σ_h and σ_v horizontal and vertical stress, respectively.

Table 1. Parameter values for the UC tests in Fig. 5 (Y_1)

σ'_{3c} (k Pa)	ν	e_{af} (%)	$(\sigma_v - \sigma_h)^*/2$ (k Pa)
100	2.5	6.4	142
200	5	5.6	228
400	15	4.4	290
800	30	3.8	363

The *UE* experimental curves in their post-peak region indicate they are of the post-peak ductility function plus the pre-peak sensitivity function $Y_D + Y_S$. Equations (3) and (1) were applied in the form

$$\sigma_1 - \sigma_3 = \left(\sigma_1 - \sigma_3\right)_\infty + \left[\left(\sigma_1 - \sigma_3\right)_1 - \left(\sigma_1 - \sigma_3\right)_\infty\right]$$

$$\left(\frac{e_a}{e_{a1}}\right)^{-1/v} + \left(\sigma_1 - \sigma_3\right)_f \left[1 + \left(\frac{e_a}{e_a^*}\right)^{-1/v_S}\right]^{-1} \tag{6}$$

where the subscript s in v_S in the third term is to distinguish it from v in the second term. As the experimental curve indicates $v_S < 1$ in the third term the parameters in the second term may be guessed from the first part of the post-peak curves and the parameters of the third term from the final part of the experimental curves. After a trial and error procedure the author found the values shown in Table 2. Theoretical points have been marked in Fig. 5. Graphs showing the variation of these parameters with σ^1_{3c} are not included. Similar graphs for all other cases will not be included due to space limitation. The pre-peak response of these *UE* tests are of the Y_S type but the author did not intended to apply such an equation due to the very poor data he could obtain from such graphs. Something similar happened with all further figures in this paper.

Table 2. Parameter values for the UE tests in Fig. 5 ($Y_D + Y_S$)

σ'_{3c} (k Pa)	ν	e_{a1} (%)	$(\sigma_v - \sigma_h)_1/2$ (k Pa)	$(\sigma_v - \sigma_h)_\infty/2$ (k Pa)	ν_S	e^*_a (%)	$(\sigma_v - \sigma_h)_f/2$ (k Pa)
100	2	-1	-10	0	0.5	-6	-45
200	2	-1	-60	0	0.5	-6	-130
400	2	-1	-120	0	0.5	-6	-180
800	2	-1	-195	0	0.5	-6	-230

A series of undrained tests using the hallow cylinder torsional shear device was carried out on the sand consolidated to essencially identical void ratios (very loose) but different initial stress states characterised by $\sigma'_{mc} = (\sigma'_{1c} + \sigma'_{2c} + \sigma'_3)/3$, $K_c = \sigma'_{1c}/\sigma'_{3c}$, $b_c = (\sigma_{2c} - \sigma_{3c})/(\sigma_{1c} - \sigma_{3c})$ and α_{oc} = inclination of the mayor principal stress to the vertical direction, perpendicular to the bedding planes.

The sand was sheared undrained while keeping α_σ (= $\alpha_{\sigma c}$), b(= b_c = 0.4), and σ_m (= σ_{mc} = 200*kPa*) constant. Fig. 6 shows the response of loose Fraser River sand consolidated to an initial stress ratio of K_c = 1.50 and α_σ ranging from 0° to 90°.

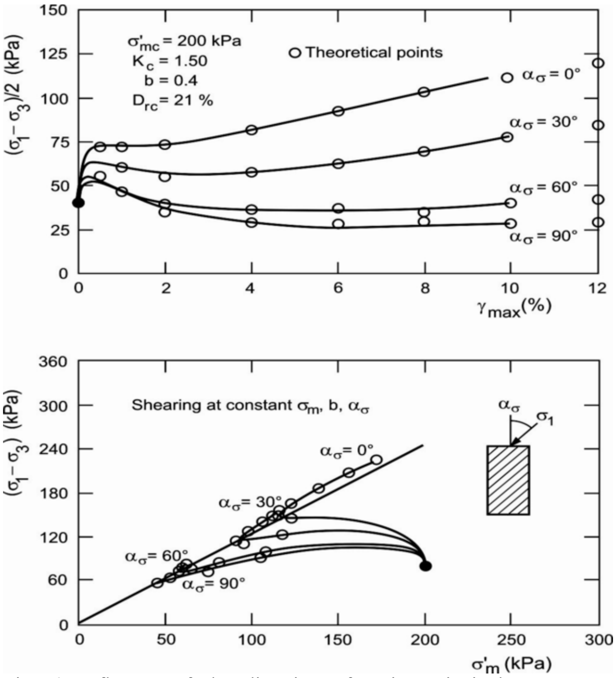

Fig. 6. Influence of the direction of major principal stress on the undrained behaviour at an initial static shear of K_c = 1.50. γ_{max}, maximum shear strain (after Sivathayalan and Vaid 2002).

The stress-strain curves in Fig. 6 indicate a behaviour of the type $Y_D + Y_S$ in their post-peak region. Consequently the equation to apply is just (6) in the form:

$$(\sigma_1 - \sigma_3)/2 = (\sigma_1 - \sigma_3)_\infty/2 + \left[(\sigma_1 - \sigma_3)_1/2 - (\sigma_1 - \sigma_3)_\infty/2\right] \left(\frac{\eta}{\eta_1}\right)^{-1/v} + (\sigma_1 - \sigma_3)_f/2\left[1 + \left(\frac{\eta}{\eta^*}\right)^{-1/v_S}\right]^{-1} \quad (7)$$

where $\eta = \eta_{max}$ = maximum shear natural strain. Equation (7) was applied considering that the Cauchy common shear strain γ_{max} is very close to η_{max} due to their small values (γ_{max} < 10%). The procedure to find the different parameters was very similar to the one used for the *UE* test in Fig. 5. After some trial and error the author found the values contained in Table 3. Theoretical points have been marked in Fig. 6.

Table 3. Parameter values for the shear tests in Fig. 6

α_σ	ν	η_1 (%)	$(\sigma_1 - \sigma_3)_1/2$ (*k Pa*)	$(\sigma_1 - \sigma_3)_\infty/2$ (*k Pa*)	ν_S	η^* (%)	$(\sigma_1 - \sigma_3)_f/2$ (*k Pa*)
0°	2	1	72	70	0.5	10	84
30°	2	1	60	35	0.5	10	70
60°	2	1	45	20	0.5	10	25
90°	2	1	45	10	0.5	10	15

From Fig. 6, the author determined the experimental pore-pressures Δu as function of the shear strain η and applied (5) to such experimental curves. As the shear tests were made at σ_m = constant the isotropic stress increment is zero and (5) was applied in the form

$$\Delta u = \alpha\sigma_{co}\left[1 + \left(\frac{\eta}{\eta^*}\right)^{-\beta}\right]^{-1} - \alpha_e(\sigma_{eo} - \sigma_{co})\left[1 + \left(\frac{\eta}{\eta_e^*}\right)^{-\beta_e}\right]^{-1} \quad (8)$$

where $\sigma_{co} = \sigma'_{mc}$ and again the sub-indexes *e* in the second term are only to distinguish them from the parameters in the first term. After some trial and error procedure taking into account Fig. 4 the pore pressure parameters found appear in Table 4. Values of σ_{eo}/σ_{co} are a measure of interlocking. Observe how these values decrease with α_σ. Theoretical points have been marked in Fig. 6 for shear strains equal to 1, 2, 4, 6, 8 and 10%. (Few of them superimpose in former ones).

Table 4. Pore pressure parameters for Fig. 6

α_σ	σ_{co} (*k Pa*)	α	β	η^* (%)	α_e	β_e	η^*_e	σ_{eo} (*k Pa*)
0°	200	1	1	1	1	1	15	590
30°	200	1	1	1	1	1	15	440
60°	200	1	1	1	1	1	15	310
90°	200	1	1	1	1	1	15	260

Comparative behaviour of loose Fraser River sand consolidated to identical $\alpha_{\sigma c}$ = 0° but different K_c values is illustrated in Fig. 7 (a). The behaviour of sand similar to that in Fig. 7 (a) but consolidated to higher $\alpha_{\sigma c}$ values of 30°, 60° and 90° is shown in Figs. 7 (b), 7 (c) and 7 (d), respectively.

Again, the stress strain curves in their post-peak regions indicate they are of the type $Y_D + Y_S$ and consequently equation (7) is the one to be applied. One important feature of these curves for each case is that they appear to be parallel. Proceeding in the same way described for the other cases and with the experience of the values for the different parameters, the author arrived to the parameter's values shown in Table 5.

Theoretical points have been marked in Fig. 7. Observe that the difference between $(\sigma_1 - \sigma_3)_1/2$ and $(\sigma_1 - \sigma_3)_\infty/2$ for each α_σ is constant and with $(\sigma_1 - \sigma_3)_f/2$ constant for each α_σ makes the curves parallel for each α_σ. The pore pressure parameters appear in Table 6. Theoretical points have been marked in Fig. 7 at shear strains of 1, 2, 4, 6, 8 and 10% for K_c = 1.00 and 2.00.

Fig. 8 shows the undrained response of sand consolidated initially to an axisymmetric stress state with different levels of static shear and subsequently sheared undrained. The undrained stress part involved rotation of the principal stress direction in addition to increasing shear stress. The mean normal stress σ_m = 200 *kPa* and the intermediate principal stress parameter b = 0 were maintained constant, but the deviator stress was increased and the direction of mayor principal stress was rotated (by $\Delta\alpha_\sigma$) simultaneously, such that the ratio $\Delta\alpha_\sigma/\Delta\sigma_{dn}$ was constant during shear. The incremental deviator stress $\Delta\alpha_d$ was normalised by the effective mean normal consolidation stress (a constant 200 *kPa* in all tests) to yield $\Delta\alpha_{dn}$, to render the degree of principal stress rotation $\Delta\alpha_\sigma/\Delta\sigma_{dn}$ a dimensional parameter.

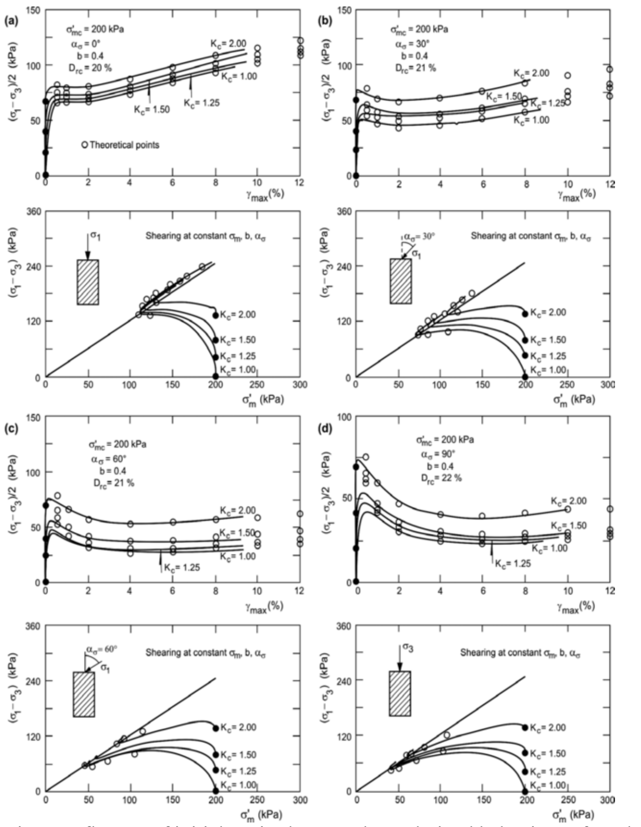

Fig. 7. Influence of initial static shear on the undrained behaviour of sands consolidated to α_c = 0º (a), 30º (b), 60 º (c), and 90º (d) (after Sivathayalan and Vaid 2002)

Table 5. Parameter values for the shear tests in Fig. 7

α_σ	K_c	ν	η_1 (%)	$(\sigma_1 - \sigma_3)_1/2$ (*k Pa*)	$(\sigma_1 - \sigma_3)_\infty/2$ (*k Pa*)	ν_S	η^* (%)	$(\sigma_1 - \sigma_3)_f/2$ (*k Pa*)
0°	1.00	2	1	66	61	0.5	10	80
	1.25	2	1	69	64	0.5	10	80
	1.50	2	1	73	68	0.5	10	80
	2.00	2	1	80	75	0.5	10	80
30°	1.00	2	1	46	26	0.5	10	70
	1.25	2	1	53	33	0.5	10	70
	1.50	2	1	56	36	0.5	10	70
	2.00	2	1	70	50	0.5	10	70
60°	1.00	2	1	40	5	0.5	10	35
	1.25	2	1	43	8	0.5	10	35
	1.50	2	1	50	15	0.5	10	35
	2.00	2	1	65	30	0.5	10	35
90°	1.00	2	1	42	0	0.5	10	25
	1.25	2	1	44	2	0.5	10	25
	1.50	2	1	47	4	0.5	10	25
	2.00	2	1	58	16	0.5	10	25

The post-peak stress strain graphs in Fig. 8 indicate they are of the type $Y_D + Y_S$ and therefore (7) is the equation to be applied in the form

$$\sigma_d = \sigma_{d\infty} + \left[\sigma_{d1} - \sigma_{d\infty}\right] \left(\frac{\eta}{\eta_1}\right)^{-1/\nu} + \sigma_{df}\left[1 + \left(\frac{\eta}{\eta^*}\right)^{-1/\nu_S}\right]^{-1} \tag{9}$$

The procedure to find the parameters was similar to the procedure used in the previous graphs. The values found appear in Table 7. Pore pressure parameters are contained in Table 8. Theoretical points have been marked in Fig. 8 at shear strains of 1, 2, 4, 6, 8 and 10**%.**

Table 6. Pore pressure parameters for Fig. 7

α_σ	K_c	σ_{co} (*k Pa*)	α	β	η^* (%)	α_e	β_e	η_e^* (%)	σ_{eo} (*k Pa*)
0°	1.00	200	1	1	1	1	1	15	550
	1.25	200	1	1	1	1	1	15	560
	1.50	200	1	1	1	1	1	15	590
	2.00	200	1	1	1	1	1	15	610
30°	1.00	200	1	1	1	1	1	15	370
	1.25	200	1	1	1	1	1	15	430
	1.50	200	1	1	1	1	1	15	440
	2.00	200	1	1	1	1	1	15	510
60°	1.00	200	1	1	1	1	1	15	260
	1.25	200	1	1	1	1	1	15	270
	1.50	200	1	1	1	1	1	15	310
	2.00	200	1	1	1	1	1	15	400
90°	1.00	200	1	1	1	1	1	15	250
	1.25	200	1	1	1	1	1	15	250
	1.50	200	1	1	1	1	1	15	260
	2.00	200	1	1	1	1	1	15	320

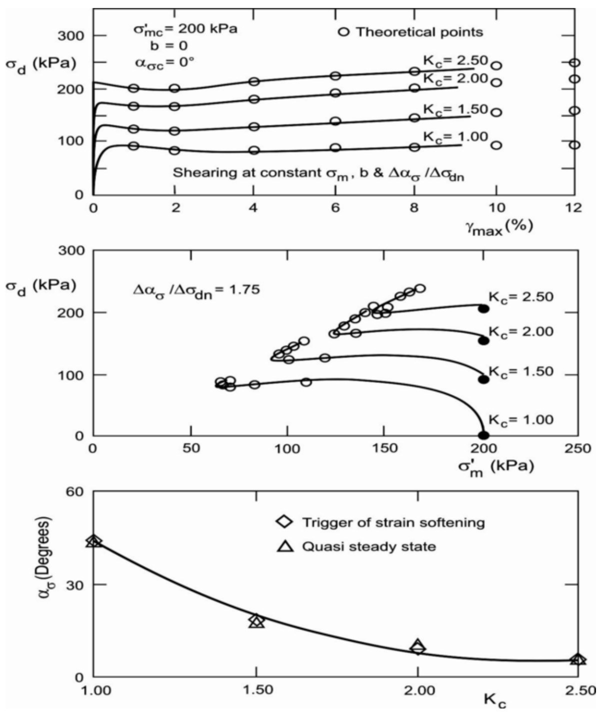

Fig. 8. Influence of initial static shear on undrained shear with principal stress rotation (after Sivathayalan and Vaid 2002)

Table 7. Parameter values for the shear tests in Fig. 8

K_c	ν	η_1 (%)	σ_{d1} ($k\,Pa$)	$\sigma_{d\infty}$ ($k\,Pa$)	ν_S	η^* (%)	σ_{df} ($k\,Pa$)
1.00	2	1	90	60	0.5	6	30
1.50	2	1	125	95	0.5	6	65
2.00	2	1	165	135	0.5	6	90
2.50	2	1	200	170	0.5	6	85

Table 8. Pore pressure parameters for Fig. 8

K_c	σ_{co} ($k\,Pa$)	α	β	η^* (%)	α_e	β_e	η_e^* (%)	σ_{eo} ($k\,Pa$)
1.00	200	1	1	1	1	1	15	330
1.50	200	1	1	1	1	1	7	350
2.00	200	1	1	1	1	1	4	375
2.50	200	1	1	1	1	1	3	395

Fig. 9 illustrates the influence of the degree of principal stress rotation (the magnitude of $\Delta\alpha_\sigma/\Delta\sigma_{dn}$) on the undrained response of anisotropically consolidated Fraser River sand. All specimens were at an identical initial state of σ'_{mc} = 200 kPa, b_c= 0, K_c = 2.00, and $\alpha_{\sigma c}$ = 0. A $\Delta\alpha_\sigma/\Delta\sigma_{dn} = \infty$ implies rotation of principal stress directions only, without any increase in maximum shear stress, whereas $\Delta\alpha_\sigma/\Delta\sigma_{dn}$ = 0 indicates no rotation of principal stress directions (constant α_σ tests).

Application of (9) was made, the values of the different parameters found appear in Table 9. Pore pressure parameters are contained in Table 10. The theoretical curve for $\Delta\alpha_\sigma/\Delta\sigma_{dn} = \infty$ was obtained from the knowledge of the maximum pore pressure Δu = 90 kPa indicated in Fig. 9.

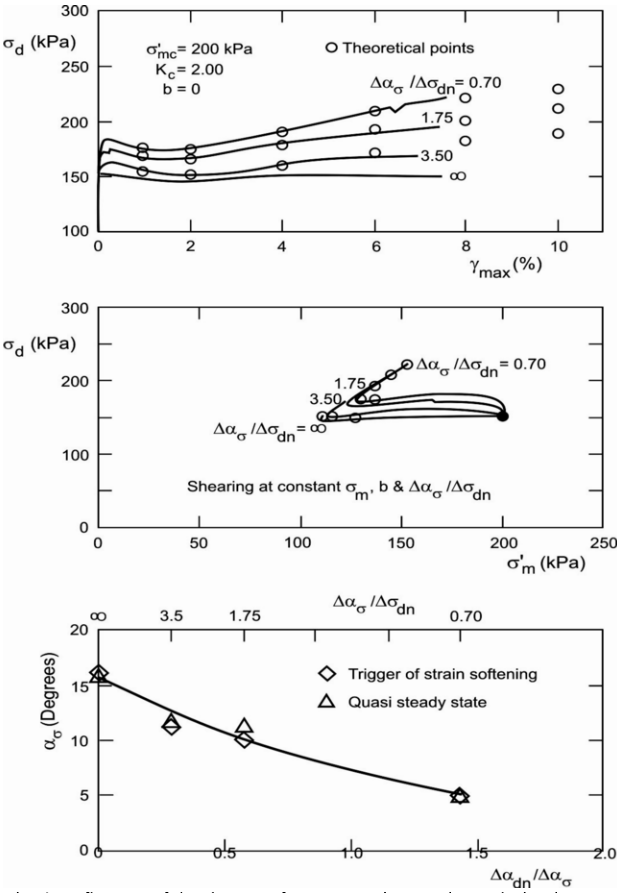

Fig. 9. Influence of the degree of stress rotation on the undrained response of sands at a given initial state (after Sivathayalan and Vaid 2002).

Table 9. Parameter values for the shear tests in Fig. 9

$\Delta\alpha_\sigma/\Delta\sigma_{dn}$	ν	η_1 (%)	σ_{d1} ($k\,Pa$)	$\sigma_{d\infty}$ ($k\,Pa$)	ν_S	η^* (%)	σ_{df} ($k\,Pa$)
0.70	2	1	170	140	0.5	6	110
1.75	2	1	165	165	0.5	6	90
3.50	2	1	150	120	0.5	6	80

Table 10. Pore pressure parameters for Fig. 9

$\Delta\alpha_\sigma/\Delta\sigma_{dn}$	σ_{co} (k Pa)	α	β	η^* (%)	α_e	β_e	η_e^* (%)	σ_{eo} (k Pa)
0.70	200	1	1	1	1	1	4	395
1.75	200	1	1	1	1	1	4	375
3.50	200	1	1	1	1	1	4	360
∞	200	1	1	1	1	1	4	340

Fig. 10 shows the behaviour of sand consolidated to identical confining static shear stresses (σ'_{mc} = 200 kPa, b_c = 0.5, K_c = 2.00) but to different initial values of α_σ and sheared undrained along a $\Delta\alpha_\sigma/\Delta\sigma_{dn} = \infty$ path. Pore pressure parameters are shown in Table 11. Theoretical points at shear strains of 1, 2, 4 and 6% have been marked in Fig. 10 for $\alpha_{\sigma c}$ = 0° and 90°.

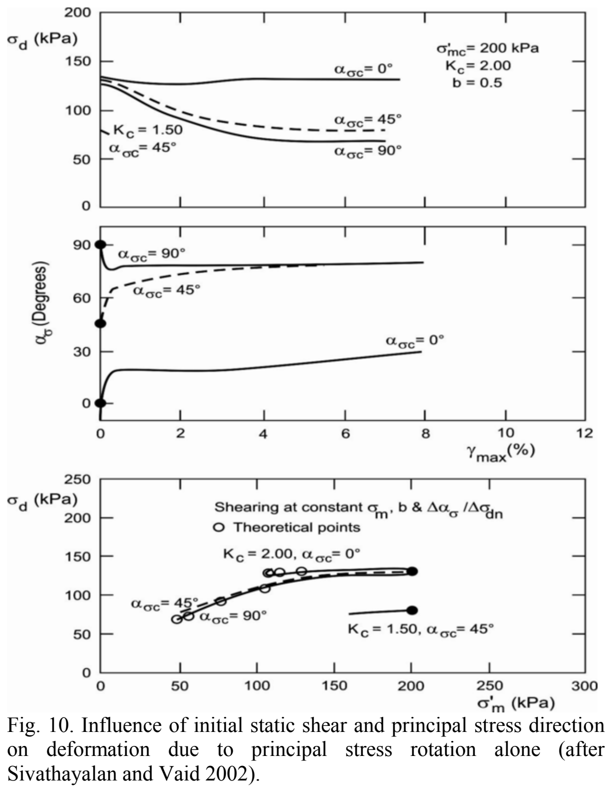

Fig. 10. Influence of initial static shear and principal stress direction on deformation due to principal stress rotation alone (after Sivathayalan and Vaid 2002).

Table 11. Pore pressure parameters for Fig. 10

$\alpha_{\sigma c}$	σ_{co} ($k\,Pa$)	α	β	η^* (%)	α_e	β_e	η_e^* (%)	σ_{eo} ($k\,Pa$)
0°	200	1	1	1	1	1	4	340
45°	200	1	1	1	1	1	4	245
90°	200	1	1	1	1	1	4	230

The undrained behaviour of sand consolidated to an identical initial state (void ratio at the end of consolidation e_c = 0.898, σ'_m = 200 kPa, b_c = 0.5, K_c = 2.00, and $\alpha_{\sigma c}$ = 30°)

and subjected to shear under an identical degree of stress rotation ($\Delta\alpha_\sigma/\Delta\sigma_{dn}$ = 1.75) under increasing and decreasing α_σ is compared in Fig. 11. Theoretical pore pressure parameters are shown in Table 12. Theoretical points have been marked in Fig. 11 for shear strains of 1, 2, 4, 6 and 8%.

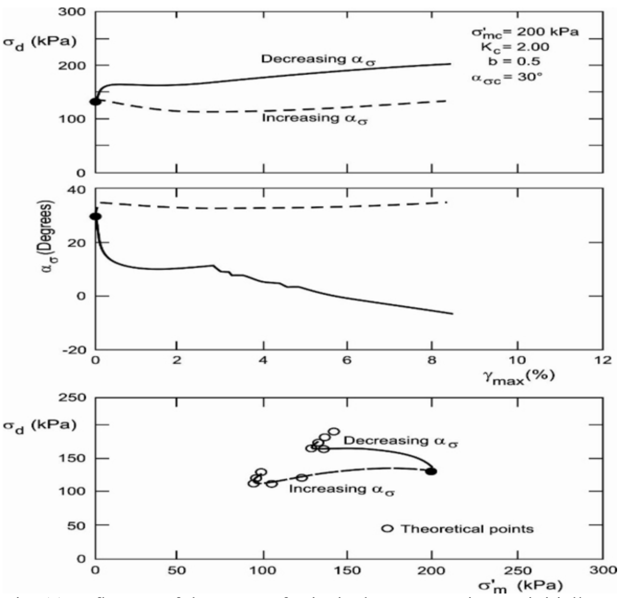

Fig. 11. Influence of the sense of principal stress rotation on initially non-axisymmetrically consolidated sand (after Sivathayalan and Vaid 2002)

Table 12. Pore Pressure parameters for Fig. 11

α_σ	σ_{co} (*k Pa*)	α	β	η^* (%)	α_e	β_e	η^*_e (%)	σ_{eo} (*k Pa*)
Decreasing	200	1	1	1	1	1	4	380
Increasing	200	1	1	1	1	1	4	310

4 CONCLUSIONS

The most important conclusions are as follows:

1. Undrained compression triaxial tests, Fig. 5, present a Y_I type of behaviour with v and $(\sigma_v - \sigma_h)^*$ increasing with σ'_{3c} (Table 1). The post-peak undrained extension triaxial tests present a $Y_D + Y_S$ type of behaviour with $v = 2$, $(\sigma_v - \sigma_h)_\infty = 0$, $v_S = 0.5$, $e^*_a = -6\%$ and $(\sigma_v - \sigma_h)$ increasing with σ'_{3c} (Table 2).
2. For the undrained shear tests using the hallow cylinder torsional shear device the stress-strain parameters that appear in Tables 3, 5, 7 and 9 for Figs. 6, 7, 8 and 9, we may conclude that the post-peak response was of the type $Y_D + Y_S$ with constant parameters $v = 2$, $v_S = 0.5$ including when there was principal stress rotation.
3. For Fig. 6, the shear tests present a constant η^* = 10% and $(\sigma_1 - \sigma_3)_f$ decreasing with α_σ (Table 3).
4. For Fig. 7, the shear tests present a constant η^* = 10% with $(\sigma_1 - \sigma_3)_f$ decreasing with α_σ but the post-peak behaviour presents parallel stress-strain curves for each α_σ = constant. (Table 5).
5. For Fig. 8, the shear tests with principal stress rotation present a constant η^* = 6% with σ_{df} increasing with K_c (Table 7).
6. For Fig. 9, the shear tests with different degree of stress rotation present a constant η = 6% with σ_{df} decreasing with $\Delta\alpha_\sigma/\Delta\sigma_{dn}$ (Table 9).
7. For the undrained shear tests using the hallow cylinder torsional shear device the pore pressure parameters that appear in Tables 4, 6, 8, 10, 11 and 12, we may conclude that the contribution of the positive pore pressure due to σ'_{3c} = 200 *kPa*, first term in equation (8), was a constant in all the tests including when the shearing was due to principal stress rotation alone. The values of the parameters were α = 1, β = 1, η^* = 1%. Furthermore, in the negative term due to interlocking of the solid particles of the sand, second term in equation (8), all the tests showed constant parameters α_e = 1 and β_e = 1. The variation was in the values of η^*_e and σ_{eo}/σ_{co}.
8. For Fig. 6, the pore pressure behaviour with different directions of the mayor principal stress presents a constant η^*_e = 15% with σ_{eo} decreasing with α_σ (Table 4).
9. For Fig. 7, the pore pressure behaviour with different initial static shears and α_σ presents a constant η^*_e = 15% with σ_{eo} decreasing with α_σ while increasing with K_c at each α_σ (Table 6).
10. For Fig. 8, the pore pressure behaviour with principal stress rotation presents decreasing values of η^*_e while increasing values of σ_{eo} with K_c (Table 8).
11. For Fig. 9, the pore pressure behaviour with different degrees of stress rotation presents a constant η^*_e = 4% with decreasing σ_{eo} with $\Delta\alpha_\sigma/\Delta\sigma_{dn}$ (Table 10)
12. For Fig. 10, the pore pressure behaviour due to principal stress rotation alone presents a constant η^*_e = 4% with decreasing σ_{eo} with $\alpha_{\sigma c}$ (Table 11).
13. For Fig. 11, the pore pressure behaviour due to the sense of principal stress rotation presents a constant η^*_e = 4% and higher σ_{eo} for decreasing α_σ than for increasing α_σ (Table 12).
14. From Fig. 8 (variable K_c, b = 0) with η^*_e = 4 for K_c = 2.00 (Table 8), Fig. 9 (K_c = 2.00, b = 0), Fig. 10 (K_c = 2.00, b = 0.5) and Fig. 11 (K_c = 2.00, b = 0.5) we deduce that the value of η^*_e depends on K_c and does not depend on b when there exists principal stress rotation.

REFERENCES

Juárez-Badillo, E. 1999 a. Static liquefaction of very loose sands: Discussion. *Canadian Geotechnical Journal,* 36:967-973.

Juárez-Badillo, E. 1999 b. Static liquefaction of sands under multiaxial loading : Discussion. *Canadian Geotechnical Journal*, 36:974-979.

Sivathayalan, S., and Vaid Y. P. 2002. Influence of generalized initial state and principal stress rotation on the undrained response of sands. *Canadian Geotechnical Journal*, 39:63-76

Vaid Y. P. and Thomas, J. 1995. Liquefaction and post-liquefaction behaviour of sand. *Journal of Geotechnical Engineering*, ASCE, 121(2):163-173.